

1 **Turbulence Measurements from Compliant Moorings - Part II: Motion**

2 **Correction**

3 Levi F. Kilcher*

4 *National Renewable Energy Laboratory, Golden, Colorado, USA*

5 Jim Thomson

6 *Applied Physics Laboratory, University of Washington, Seattle, Washington, USA*

7 Samuel Harding

8 *Pacific Northwest National Laboratory, Richland, Washington, USA*

9 Sven Nylund

10 *Nortek AS, Norway*

11 *Corresponding author address: Levi Kilcher, National Renewable Energy Laboratory, 15013 Den-
12 ver West Pkwy, Golden, Colorado, USA

13 E-mail: Levi.Kilcher@nrel.gov

ABSTRACT

14 Acoustic Doppler velocimeters (ADVs) are a valuable tool for making high-
15 precision measurements of turbulence, and moorings are a convenient and
16 ubiquitous platform for making many kinds of measurements in the ocean.
17 However, because of concerns that mooring motion can contaminate turbu-
18 lence measurements and acoustic Doppler profilers make mid-depth veloc-
19 ity measurements relatively easy, ADVs are not frequently deployed from
20 moorings. This work demonstrates that inertial motion measurements can
21 be used to reduce motion-contamination from moored ADV velocity mea-
22 surements. Three distinct mooring platforms were deployed in a tidal channel
23 with inertial-motion-sensor-equipped ADVs. In each case, motion correction
24 based on the inertial measurements reduces mooring motion contamination of
25 velocity measurements. The spectra from these measurements are consistent
26 with other measurements in tidal channels, and have a $f^{-5/3}$ slope at high
27 frequencies—consistent with Kolmogorov’s theory of isotropic turbulence.
28 Motion correction also improves estimates of cross spectra and Reynold’s
29 stresses. Comparison of turbulence dissipation with flow speed and turbu-
30 lence production indicates a bottom boundary layer production-dissipation
31 balance during ebb and flood that is consistent with the strong tidal forcing
32 at the site. These results indicate that inertial-motion-sensor-equipped ADVs
33 are a valuable new tool for making high-precision turbulence measurements
34 from moorings.

35 **1. Introduction**

36 Acoustic Doppler velocimeters (ADVs) have been used to make high-precision measurements of
37 water velocity for over 20 years (Kraus et al. 1994; Lohrmann et al. 1995). During that time, they
38 have been deployed around the world to measure turbulence from a range of platforms, including
39 the laboratory setting (Voulgaris and Trowbridge 1998), from stationary structures on ocean-, river-
40 and lake-bottoms (Kim et al. 2000; Lorke 2007; Cartwright et al. 2009), in surface waters from
41 a pole lowered from a ship's bow (Geyer et al. 2008), and in the deep ocean from autonomous
42 underwater vehicles (e.g., Zhang et al. 2001; Goodman et al. 2006).

43 A relatively small fraction of ADV measurements have been made from moorings (e.g., Fer and
44 Paskyabi 2014). Presumably this is because mooring motion can contaminate ADV measurements,
45 and acoustic Doppler profilers (ADPs) can measure some mid-depth turbulence statistics without
46 a mooring (e.g., Stacey et al. 1999a; Rippeth et al. 2002; Wiles et al. 2006; Guerra Paris and
47 Thomson 2017). Still, ADV measurements have distinct characteristics that can be advantageous:
48 they are capable of higher sample rates, have higher signal-to-noise ratios, and have a much smaller
49 sample volume (1 centimeter, as opposed to several meters).

50 Inertial motion unit (IMU) sensors have been used in the aerospace and aeronautical industries
51 to quantify the motion of a wide range of systems, and to improve atmospheric velocity measure-
52 ments, for several decades (Axford 1968; Edson et al. 1998; Bevly 2004). In the last decade, the
53 smartphone, drone, and ‘Internet of Things’ markets have driven innovation in microelectrical-
54 mechanical systems, including the IMU. As a result of this growth and innovation, the cost, power
55 requirements, and size of IMUs have come down. These changes have allowed these sensors to be
56 integrated into oceanographic instruments that have small form-factors, and rely on battery power.

57 Nortek now offers a version of their Vector ADV with a Microstrain 3DM-GX3-25 IMU sen-
58 sor (Nortek 2005; MicroStrain 2012). This IMU's signals are incorporated into the Vector data
59 stream so that its motion and orientation signals are tightly synchronized with the ADV's velocity
60 measurements. The tight synchronization provides a dataset that can be utilized to quantify ADV
61 motion in the Earth's inertial reference frame, and remove that motion from the ADV's velocity
62 measurements at each time step of its sampling (Edson et al. 1998). This work utilizes 'ADV-IMU'
63 measurements from mid-depth moorings in Puget Sound to demonstrate that motion correction can
64 improve the accuracy of oceanic turbulence spectra, turbulence dissipation, and Reynolds stress
65 estimates.

66 This effort was originally motivated by a need for low-cost, high-precision turbulence measure-
67 ments for the emerging tidal energy industry (McCaffrey et al. 2015; Alexander and Hamlington
68 2015). Experience in the wind energy industry has shown that wind turbine lifetimes are reduced
69 by atmospheric turbulence, and the same is expected to be true for tidal energy turbines. In the
70 atmosphere, meteorological towers are often used to position sonic anemometers at the hub height
71 of wind turbines for measuring detailed turbulence inflow statistics (Hand et al. 2003; Kelley et al.
72 2005; Mücke et al. 2011; Afgan et al. 2013). In the ocean, tower-mounted hub-height turbulence
73 measurements have been made, but they are challenging to install and maintain in energetic tidal
74 sites (Gunawan et al. 2014; Thomson et al. 2012). Therefore, the U.S. Department of Energy
75 funded this work to investigate the accuracy of mooring-deployed ADV-IMUs to reduce the cost
76 of turbulence measurements at tidal energy sites (Kilcher et al. 2016). The approach proved to be
77 successful and potentially useful to the broader oceanographic community interested in moored
78 turbulence measurements (Lueck and Huang 1999; Doherty et al. 1999; Nash et al. 2004; Perlin
79 and Moum 2012; Alford 2010; Paskyabi and Fer 2013).

80 The next section describes details of the measurements, including a summary of the hardware
81 configurations (platforms) that were used to support and position the ADV-IMUs in the water
82 column. A detailed description of the motion of these platforms is found in the companion paper
83 to this work, Harding et al. (2017), hereafter Part 1. Section 3 describes the mathematical details
84 of motion correction and Section 4 presents results from applying the method to measurements
85 from the various platforms. Section 5 is a discussion of the energetics of the tidal channel in
86 which the measurements were made and demonstrates that the measurements are consistent with
87 turbulence theory and other measurements in similar regimes. A summary and concluding remarks
88 are provided in Section 6.

89 **2. Measurements**

90 This work focuses on measuring turbulence from ADVs that are equipped with IMUs and de-
91 ployed from moving (moored) platforms. The ADVs utilized for these measurements were Nortek
92 Vector ADVs equipped with Microstrain 3DM-GX3-25 IMUs. These IMUs captured all six com-
93 ponents of ADV motion (three components of angular rotation and three components of linear
94 acceleration), as well as the orientation of the ADV pressure case. The IMU measures its motion
95 at 1 kHz and uses internal signal integration (Kalman filtering) to output the motion signals at
96 the same sample rate as the ADV's velocity measurements (the measurements are synchronized to
97 within 10^{-2} s). This reduces aliasing of the IMU's motion measurements above the ADV's sample
98 rate (MicroStrain 2010).

99 All measurements used in this work were made in Admiralty Inlet, Washington, approximately
100 500 m west southwest of Admiralty Head in 60 m of water at $48^{\circ} 9.18' \text{ N}$, $122^{\circ} 41.22' \text{ W}$ (Figure
101 1). The site is approximately 6 km east of Port Townsend. Admiralty inlet is the largest waterway
102 connecting Puget Sound to the Strait of Juan de Fuca, and it possesses a large semidiurnal tidal flow

¹⁰³ (Thomson et al. 2012; Polagye and Thomson 2013). This work utilizes data from three distinct
¹⁰⁴ deployment platforms: the tidal turbulence mooring, a StableMoor buoy, and a sounding weight.
¹⁰⁵ Each of these platforms are briefly described below, and additional details, photos, and schematic
¹⁰⁶ diagrams can be found in Part 1. This entire work—including manuscript source text, source data,
¹⁰⁷ figures, and analysis scripts—are publicly available (Kilcher et al. 2017).

¹⁰⁸ *a. Tidal Turbulence Mooring*

¹⁰⁹ The tidal turbulence mooring (TTM) is a simple mooring system with a strongback fin sus-
¹¹⁰ pended between a steel clump-weight anchor weighing 1,200 kg when dry and a 0.93-m-diameter
¹¹¹ spherical steel buoy with a buoyancy of 320 kg. The ADV pressure cases were clamped to one
¹¹² side of the strongback fin and the ADV sensor head was positioned 10 cm in front of the fin’s
¹¹³ leading edge (Figure 2). The leading edge of the fin is fastened inline with the mooring line. This
¹¹⁴ configuration was designed to work like a weather vane, such that the drag on the fin held the ADV
¹¹⁵ head upstream of the mooring components. This work utilizes data from two TTM deployments.

¹¹⁶ The first TTM deployment was from 1730 local time (LT) 12 June 2012 until 1430 LT 14 June
¹¹⁷ 2012. Two Nortek ADVs were clamped to either side of the fin so that the axis of their cylindrical
¹¹⁸ pressure cases were parallel with the leading edge of the strongback. The ADV heads were spaced
¹¹⁹ 0.5 m apart vertically along the fin. Only one of these ADVs was equipped with an integrated
¹²⁰ IMU. This TTM also had an upward-looking ADP mounted on the mooring anchor.

¹²¹ Periods of time during which this mooring interfered with a beam of the ADP were identified
¹²² by inspecting the profiler’s acoustic amplitude signal. Periods during which one beam of the
¹²³ profiler had > 5% higher acoustic amplitude than the other beams were flagged as “contaminated”
¹²⁴ and excluded from averaging. Five-minute averages in which more than 50% of the data were
¹²⁵ contaminated in this way were masked as invalid.

126 The second TTM deployment was from 0600 LT 17 June 2014 to 0500 LT 19 June 2014. Two
127 Nortek ADV-IMUs were mounted on this TTM, with their heads spaced 0.5 m apart along the fin.
128 In this case, the pressure cases and ADV heads were inclined at an angle of 18° from normal to
129 the leading edge of the fin to account for mooring blowdown during strong currents (Figure 3).
130 This change was made to reduce vibrational motion observed during the June 2012 deployment
131 that was believed to be associated with the orientation of the pressure cases. There was no ADP on
132 the anchor of this TTM.

133 *b. The StableMoor platform*

134 The second deployment platform was a cylindrical, StableMoorTM, syntactic foam buoy (man-
135 ufacturer: Deep Water Buoyancy) that was anchored to a clump weight that weighed 1,200 kg
136 (Figure 4). The buoy is 3.5 m long and 0.45 m in diameter with a tail ring that is 0.76 m in diame-
137 ter. The StableMoor buoy (hereafter, ‘SMB’) weighs 295 kg in air, and has a buoyancy of 185 kg
138 in water.

139 The SMB was deployed with an ADV-IMU mounted at its nose from 11:21 on May 12 to 11:53
140 on May 13, 2015 (local time). The sample volume of the ADV is 10 cm forward of the nose and 20
141 cm above the center line of the SMB (Figure 4). Based on Wyngaard et al.’s (1985) investigation
142 of a similarly shaped slender body, the velocity measurements should have flow-distortion effects
143 of less than 10%. The SMB was equipped with a 1,200-kHz RDI workhorse sentinel ADP that
144 was oriented downward-looking to measure water velocity below the platform in twelve 1-m bins
145 and measure platform motion (“bottom tracking”), all at a 1-Hz sample rate.

146 The SMB has two primary advantages compared to the TTM. First, it is significantly more
147 massive and hydrodynamically stable than the TTM, which reduces the frequency of motions of
148 the platform (Part I). Second, the SMB is capable of supporting a bottom-tracking ADP, which

¹⁴⁹ provides an independent measure of the platform's translational motion. Disadvantages of the
¹⁵⁰ SMB include: its size, which adds to the challenge of deployment and recovery, and its cost,
¹⁵¹ which is significantly higher than the TTM system.

¹⁵² *c. Turbulence Torpedo*

¹⁵³ The turbulence torpedo is a simple sounding weight with an ADV head mounted forward of the
¹⁵⁴ nose, and the ADV pressure case strapped below (Figure 5). This platform was deployed on May
¹⁵⁵ 14, 2015, for 37 minutes starting at 07:41 local time. This measurement was made from a davit
¹⁵⁶ that hung the system from the side of the ship to a depth of approximately 25 m. The primary
¹⁵⁷ advantages of this platform are its compact size, low cost, and the flexibility to perform spatial
¹⁵⁸ transects.

¹⁵⁹ *d. Coordinate system and turbulence averaging*

¹⁶⁰ Unless stated otherwise, vector quantities in this work are in a fixed "principal-axes" coordinate
¹⁶¹ system that is aligned with the bidirectional tidal flow: positive u is in the direction of ebb (310°
¹⁶² True), positive w is vertically upward, and v is the cross-stream component in a right-handed
¹⁶³ coordinate system (Figure 1). The full velocity vector, $\tilde{\mathbf{u}} = (\tilde{u}, \tilde{v}, \tilde{w})$, is separated into a mean and
¹⁶⁴ turbulent component as $\tilde{\mathbf{u}} = \bar{\mathbf{u}} + \mathbf{u}$, where the over-bar denotes a 5-minute average. Turbulence
¹⁶⁵ kinetic energy, $tke = \overline{u^2} + \overline{v^2} + \overline{w^2}$, and Reynold's stresses, \overline{uv} , \overline{uw} , \overline{vw} , are also estimated using
¹⁶⁶ a 5-minute average. The horizontal velocity magnitude is computed as, $\bar{U} = (\bar{u}^2 + \bar{v}^2)^{1/2}$. The
¹⁶⁷ friction velocity is estimated as, $u_* = (\overline{uw^2} + \overline{vw^2})^{1/4}$; note that this is taken at the height of the
¹⁶⁸ ADV measurements, and should therefore only be interpreted as a proxy for the friction velocity
¹⁶⁹ at the bottom boundary.

170 All spectra, $S\{x\}(f) = |\mathcal{F}\{x(t)\}|^2$, and cross spectra, $C\{x,y\}(f) = \text{real}(\mathcal{F}\{x(t)\}\mathcal{F}\{y(t)\})$, are
171 computed using NumPy fast Fourier transform routines (van der Walt et al. 2011). Here, $\mathcal{F}\{x(t)\}$
172 denotes the fast Fourier transform of a signal $x(t)$ that has been linearly detrended and Hanning
173 windowed to reduce spectral reddening.

174 Throughout the remainder of this work, the dependence of S and C on f is implied (e.g., $S\{x\}(f)$
175 is hereafter $S\{x\}$), and for other variables the dependence on t is implied. Spectra and cross spectra
176 are normalized to preserve variance; e.g., $\int S\{u\}df = \overline{u^2}$, and $\int C\{u,v\}df = \overline{uv}$. The notations
177 $S\{\mathbf{u}\} = (S\{u\}, S\{v\}, S\{w\})$, and $C\{\mathbf{u}\} = (C\{u,v\}, C\{u,w\}, C\{v,w\})$ denote the set of spectra and
178 cross spectra for each velocity component and pairs of components, respectively.

179 Turbulence dissipation rates are computed as:

$$\varepsilon = \frac{1}{\bar{U}} \left(\alpha \left\langle (S\{u\} + S\{v\} + S\{w\}) f^{5/3} \right\rangle_{f_{IS}} \right)^{3/2} \quad (1)$$

180 where $\alpha = 0.5$ and $\langle \rangle_{f_{IS}}$ denotes an average over the inertial subrange of the velocity spectra and
181 where the signal-to-noise ratio is small (Lumley and Terray 1983; Sreenivasan 1995). Throughout
182 this work, we take this average from 0.3 to 1 Hz for the u and v components, and 0.3 to 3 Hz for
183 the w component.

184 3. Methodology

185 This work describes a method for correcting velocity measurements from a moving velocity
186 sensor, $\tilde{\mathbf{u}}_m$, using independent measurements of that sensor's motion, $\tilde{\mathbf{u}}_h$, to remove the motion
187 from the velocity measurements, and thus estimate the ‘motion corrected velocity’:

$$\tilde{\mathbf{u}}(t) = \tilde{\mathbf{u}}_m(t) + \tilde{\mathbf{u}}_h(t) \quad . \quad (2)$$

188 Note here that the ‘+’-sign is correct because head motion, $\tilde{\mathbf{u}}_h$, induces a measured velocity in
189 the opposite direction of the head motion itself ($\tilde{\mathbf{u}}_m = \tilde{\mathbf{u}} - \tilde{\mathbf{u}}_h$). This approach has been used

190 to successfully correct sonic anemometer measurements of atmospheric turbulence (e.g., Edson
 191 et al. 1998; Miller et al. 2008). In the ocean, previous works have utilized inertial motion sensors
 192 to quantify the motion of multiscale profilers for the purpose of measuring the full spectrum of
 193 oceanic shear (Winkel et al. 1996), and to quantify the motion of thermistor sensors (Moum and
 194 Nash 2009), but the Edson et al. (1998) approach has not been documented for moored ADV
 195 measurements.

196 The Microstrain IMU available in the Nortek Vector ADV measures the linear acceleration,
 197 $\mathbf{a}^*(t)$, rotational motion, $\boldsymbol{\omega}^*(t)$, and orientation matrix in the earth's reference frame, $\mathbf{R}(t)$, of the
 198 ADV at every time step of the ADV's sampling. The '*' superscripts denote that these vectors are
 199 measured in the ADV's local coordinate system. They can be rotated into the earth frame using
 200 the inverse of the orientation matrix, e.g., $\mathbf{a}(t) = \mathbf{R}^T(t) \cdot \mathbf{a}^*(t)$. The motion of the ADV head is
 201 calculated from these signals as the sum of rotational and translational motion:

$$\begin{aligned}
 \tilde{\mathbf{u}}_h &= \tilde{\mathbf{u}}_\omega + \tilde{\mathbf{u}}_\mathbf{a} + \tilde{\mathbf{u}}_{\text{low}} \\
 &= \mathbf{R}^T(t) \cdot (\boldsymbol{\omega}^*(t) \times \ell^*) + \int \langle \mathbf{a}(t) \rangle_{f_a} dt + \tilde{\mathbf{u}}_{\text{low}}(t)
 \end{aligned} \tag{3}$$

202 Here ℓ^* is the vector from the IMU to the ADV head, and the notation $\langle \cdot \rangle_{f_a}$ indicates a high-
 203 pass filtering operation at frequency f_a . The high-pass filter reduces low-frequency noise in \mathbf{a} —
 204 sometimes referred to as bias drift—that is amplified by integration (Barshan and Durrant-Whyte
 205 1995; Bevly 2004; Gulmammadov 2009). $\tilde{\mathbf{u}}_{\text{low}}$ is the low-frequency translational motion that
 206 is unresolved by $\tilde{\mathbf{u}}_\mathbf{a}$, and it is discussed in more detail below. To avoid double counting, $\tilde{\mathbf{u}}_{\text{low}}$
 207 should be estimated by applying the complementary low-pass filter (i.e., at f_a) to the independent
 208 measurement of low-frequency motion. We use fourth order, zero-phase (bidirectional), Hanning
 209 filters for all filtering operations.

210 The noise levels of the IMU, \mathbf{n}_ω and \mathbf{n}_a , are computed from ADV-IMU data collected while the
211 instrument was resting motionless on a table for several hours. Where, for this motionless dataset,
212 the noise levels are defined according to (3) with \mathbf{n}_ω in place of $\tilde{\mathbf{u}}_\omega$, and \mathbf{n}_a in place of $\tilde{\mathbf{u}}_a$.

213 For quantifying \mathbf{n}_ω we assume that $|\ell^*| = 1$, which is the approximate length of the ADV head
214 cable. $S\{\mathbf{n}_\omega\}$ is equal in all three components, because the rotation-rate sensor noise-levels are
215 independent of orientation (Figure 6, yellow). $S\{\mathbf{n}_\omega\}$ is several orders of magnitude lower than
216 the velocity spectra we measured (grey region), and also more than an order of magnitude smaller
217 than the Doppler noise levels of the ADV. This indicates that the precision of $\tilde{\mathbf{u}}_\omega$ (i.e. the angular
218 rate sensor) is adequate for making corrections to ADV velocity measurements.

219 The noise level of $S\{\tilde{\mathbf{u}}_a\}$ (Figure 6, black), on the other hand, is dominated by a f^{-2} slope
220 that results from integrating the low-frequency noise in \mathbf{a} . The horizontal (u and v) spectra of
221 these noise levels are identical, and so we only present one of them for simplicity (solid lines).
222 The vertical spectra noise levels are different because the signal-to-noise ratio is larger (dashed
223 black lines). High-pass filtering reduces the low-frequency noise (blue and red) so that it does
224 not contaminate motion correction, but any real motion that does exist at these frequencies is lost
225 (Egeland 2014; VanZwieten et al. 2015). This means there is a residual low-frequency translational
226 motion, $\tilde{\mathbf{u}}_{low}$, that needs to be measured independently—or at the very least considered—when
227 using ADV-IMU data from moving platforms.

228 For the SMB, the ADP bottom-track measured $\tilde{\mathbf{u}}_{low}$, and this measurement agrees with $\tilde{\mathbf{u}}_a$ over
229 a narrow frequency band (see Part I, appendix A), indicating that the ADP and IMU are resolving
230 the same motion. When this is the case, it is trivial to select a frequency in the middle of the
231 spectral overlap (in this case, we choose $f_a = 0.2$ Hz), and high-pass and low-pass filter $\tilde{\mathbf{u}}_a$ and
232 $\tilde{\mathbf{u}}_{low}$, respectively, then sum to estimate total translational motion.

233 The position of the TTM ADV can be estimated, relative to its anchor, by assuming the moor-
234 ing acts like a rigid pole and using the IMU orientation matrix to estimate the pole’s ‘lean’. The
235 position obtained from this model can then be differentiated to estimate $\tilde{\mathbf{u}}_{\text{low}}$ (this model does not
236 apply at high frequencies). Spectra of $\tilde{\mathbf{u}}_{\text{low}}$ estimated using this approach for the June 2014 TTM
237 deployment (Figure 6, green) are plotted up to the point where they cross their respective $S\{\tilde{\mathbf{u}}_{\mathbf{a}}\}$
238 noise level (black). Together, these two lines provide an ‘aggregate noise level’ of translational ve-
239 locity estimates for the TTM: the rigid pole estimate of $\tilde{\mathbf{u}}_{\text{low}}$ indicates the amplitude of unresolved
240 motion at low- f (green), and $S\{\tilde{\mathbf{u}}_{\mathbf{a}}\}$ indicates the limits of the IMU at high- f (black). Coinciden-
241 tally, $S\{\langle \tilde{\mathbf{u}}_{\mathbf{a}} \rangle_{0.03\text{Hz}}\}$ is not a terrible approximation for this aggregate noise level. Furthermore,
242 because this aggregate noise level is at least a factor of 4 smaller than the velocity spectra we
243 measured (shaded region), the results of motion correction are not sensitive to whether we use the
244 rigid pole model to estimate $\tilde{\mathbf{u}}_{\text{low}}$, or if we simply assume that $\tilde{\mathbf{u}}_{\text{low}} = 0$.

245 The choice of f_a does influence the effectiveness of motion correction (Figure 7). When f_a is
246 too high (e.g., 0.3 Hz, red), the high-pass filter removes resolved motion from $\tilde{\mathbf{u}}_h$ that could be
247 used to correct velocity measurements. In particular, notice that the amplitude of the 0.15 Hz
248 peak—which is clearly the result of motion contamination (grey line)—is reduced significantly
249 when we preserve more $\tilde{\mathbf{u}}_h$ information by reducing the high pass filter frequency to $f_a = 0.03$ Hz.
250 Further reducing f_a to 0.003 Hz does not reduce the peak further, but does increase the amplitude
251 of the spectra at low-frequency. This increase is the IMU-accelerometer’s low-frequency bias drift
252 (Figure 6) contaminating the velocity measurements. Therefore, we conclude that $f_a = 0.03$ Hz is
253 a convenient ‘middle’ frequency that reduces accelerometer bias-drift without destroying resolved
254 motion of the TTM. The same $f_a = 0.03$ Hz filter was selected, based on a similar analysis, for the
255 turbulence torpedo.

256 Thus, we find that filter selection involves a trade-off between filtering out the bias drift noise
257 at low-frequencies while not filtering out measured motion at high frequencies. In general, this
258 will depend on the dynamics of the platform used to support the ADV, and the intensity of the
259 turbulence being measured. When an independent measurement of $\tilde{\mathbf{u}}_{\text{low}}$ is available the cross-
260 coherence with $\tilde{\mathbf{u}}_a$ can indicate a region of spectral overlap, and f_a can be selected at the midpoint.
261 Lacking a reliable estimate of $\tilde{\mathbf{u}}_{\text{low}}$, the value of f_a that produces the lowest tke estimates is likely
262 the best.

263 Additional details on motion correction—including a detailed accounting of the distinct co-
264 ordinate systems of the IMU, ADV pressure case, and ADV head—can be found in Kilcher
265 et al. (2016). Open-source Python tools for performing motion correction of ADV-IMU data—
266 including scripts that write processed data in Matlab and tabulated formats—are available at
267 <http://lkilcher.github.io/dolfin/>.

268 4. Results

269 a. Mean velocity

270 Figure 8 shows a comparison of $\bar{\mathbf{u}}$ measured by an ADV-IMU mounted on the TTM, to an
271 upward-looking ADP on the anchor. The profiler measurements—taken at the same depth as
272 the ADV on the TTM—were contaminated by acoustic reflection from the strongback fin when
273 it was inline with one of the profiler’s beams (see section 2.a). When those points (not shown
274 in the figure) are excluded, this comparison shows excellent agreement between the ADV and
275 ADP measurements of mean velocity. The \bar{u} , \bar{v} , and \bar{w} components have a root-mean-square error
276 of 0.05, 0.13, and 0.03 ms^{-1} , respectively. Although it is important to note that there is some
277 discrepancy between ADP- and ADV-measured velocities (especially in \bar{v} , which is most likely

278 due to incomplete motion correction), the agreement between the magnitude and direction of these
279 independent velocity measurements indicates that moored ADV-IMUs provide a reliable estimate
280 of mean velocity in the Earth's reference frame.

281 *b. TTM spectra*

282 As discussed in detail in Part 1, the mooring motion of the TTM, $S\{\mathbf{u}_h\}$, has a peak at 0.1 to 0.2
283 Hz from swaying of the mooring that is most likely driven by eddy shedding from the spherical
284 buoy (Figure 9, red lines). There is also higher-frequency broadband motion that is associated with
285 fluttering of the strongback fin around the mooring line. These motions are especially energetic
286 in $S\{v\}$ because this is the direction in which the TTM is most unstable. As is expected from
287 fluid-structure interaction theory, the amplitude of these motions increases with increasing mean
288 velocity (Morison et al. 1950).

289 The mooring motion contaminates the uncorrected ADV measurements of velocity, $S\{\mathbf{u}_m\}$,
290 whenever the amplitude of the motion is similar to or greater than the amplitude of the turbulence.
291 Fortunately, much of this motion can be removed as detailed in Section 3. At high frequencies
292 ($f > 0.3$ Hz) for each mean-flow speed $S\{\mathbf{u}\}$ are consistent with Kolmogorov's (1941) theory of
293 isotropic turbulence: the spectra decay with a $f^{-5/3}$ slope and have equal amplitude across the ve-
294 locity components. At lower frequencies, the spectral 'roll-off' shape is similar to that measured
295 by several others (e.g., Thomson et al. 2012; McMillan et al. 2016). The degree of agreement
296 between Kaimal et al.'s (1972) semi-empirical form (cyan) and $S\{\mathbf{u}\}$ is similar to that of Walter
297 et al. (2011). This suggests that bottom-boundary layer physics are contributing to the turbulence
298 at this site and depth.

299 For $|\mathbf{u}| > 1.0 \text{ ms}^{-1}$, motion correction improves $S\{u\}$ and $S\{v\}$ at frequencies as high as 3
300 Hz. This indicates that tight synchronization between the ADV and IMU is important and that
301 implementing asynchronous approaches to motion correction may be challenging.

302 As successful as motion correction is, some motion contamination is ‘persistent’. This is most
303 notable in $S\{v\}$ at the highest flow speeds ($> 2.0 \text{ ms}^{-1}$): a peak at 0.15 Hz is an order of magnitude
304 larger than a smooth spectral shape would suggest. This persistent motion contamination is evident
305 to a lesser degree in $S\{u\}$ for $|u| > 2 \text{ ms}^{-1}$, and in $S\{v\}$ at lower flow speeds. $S\{w\}$ appears to
306 have no persistent motion contamination because the amplitude of the motion in this direction is
307 much lower than the measured spectra.

308 The amplitude of the persistent motion contamination peaks in $S\{v\}$ at 0.15 Hz is a factor of 5 to
309 10 times smaller than the amplitude of the ADV head motion itself. This observation suggests that
310 the Microstrain IMU can be used to effectively correct mooring motion at this frequency when the
311 amplitude of that motion is less than 5 times the amplitude of the real turbulence spectrum. As a
312 result, we have chosen a value of 3 as a conservative estimate of motion correction’s effectiveness.

313 In addition to the primary benefit of correcting for mooring motion, the IMU measurements
314 can also be used to identify and screen out persistent motion contamination. For example, one
315 of the most common uses of turbulence spectra is for the calculation of ε and tke. For these
316 purposes, and based on the relative amplitudes of the 0.15-Hz peaks, we assume that persistent
317 motion contamination is likely where $S\{\mathbf{u}_h\}/S\{\mathbf{u}\} > 3$, and thereby exclude these regions from
318 spectral fits.

319 In the present case, for u - and w -component spectra, this criteria only excludes a narrow range of
320 frequencies at the 0.15-Hz motion peak for the largest flow speeds. This criteria is more restrictive
321 of v -component spectra at high frequencies for $\bar{U} > 1.0 \text{ ms}^{-1}$, but this may be acceptable because

322 the amplitude of $S\{v\}$ at these frequencies—i.e., in the isotropic inertial subrange—should be
323 equal to that of $S\{u\}$ and $S\{w\}$ (Kolmogorov 1941).

324 Agreement of $S\{v\}$ with that of $S\{u\}$ and $S\{w\}$ at frequencies > 0.3 Hz indicates that motion
325 correction is effective at those frequencies even when $S\{\mathbf{u}_h\}/S\{\mathbf{u}\} \gtrsim 3$. This outcome suggests
326 that our screening threshold is excessively conservative at those frequencies, and that a more pre-
327 cise screening threshold may be frequency dependent. For example, it might take into account the
328 f^{-2} character of the noise in $S\{\mathbf{u}_a\}$ (Figure 6). For the purpose of this work, the $S\{\mathbf{u}_h\}/S\{\mathbf{u}\} < 3$
329 threshold for spectral fits is sufficient, and detailed characterization of the IMU’s motion- and
330 frequency-dependent noise level is left for future work.

331 *c. StableMoor Spectra*

332 Spectra of SMB motion have broader peaks, with a maximum amplitude that is approximately
333 half the frequency of the TTM spectral peak (0.06 Hz, Figure 10). The motion of this platform also
334 does not have high-frequency “subpeaks” or other high-frequency broadband excitation (Part 1).
335 These characteristics are due to the more massive and hydrodynamically streamlined properties of
336 the SMB compared to the TTM.

337 Like the TTM, the motion-corrected spectra from the SMB are consistent with turbulence theory
338 and previous observations. A notable distinction from the TTM, however, is that there are no
339 obvious persistent motion contamination peaks. That is, this measurement system provides an
340 accurate estimate of the turbulence spectra at this location from low frequencies to more than 1
341 Hz—well into the inertial subrange—for all three components of velocity.

342 Note that this level of accuracy cannot be obtained without the independent estimate of \mathbf{u}_{low}
343 (from the bottom-tracking ADP). If we assume that $\mathbf{u}_{low} = 0$, a similar plot to Figure 10 (not
344 shown) reveals persistent motion-contamination peaks and troughs in $S\{u\}$ and $S\{v\}$ regardless

345 of the choice of f_a . This indicates that the low-frequency translational motion of the SMB that
346 is important to motion correction is poorly resolved by the IMU's accelerometer. In other words,
347 compared to the TTM, the SMB provides a more accurate measurement of turbulence when it
348 includes an independent measure of \mathbf{u}_{low} , but it does no better—and perhaps worse—when it does
349 not.

350 *d. Torpedo spectra*

351 $S\{u_h\}$ and $S\{v_h\}$ for the turbulence torpedo is broadband and $S\{w_h\}$ motion has a narrow peak
352 at 0.3 Hz (Figure 11). Because \mathbf{u}_h is estimated using $f_a = 0.03$ Hz and assuming $\mathbf{u}_{\text{low}} = 0$, its
353 spectra rolls off quickly below f_a . Motion correction of the torpedo data appears to effectively
354 remove a motion peak from $S\{w\}$ at 0.3 Hz, and corrects $S\{v\}$ between 0.04 and 0.6 Hz. $S\{u\}$
355 is mostly unaffected by motion at these frequencies, because the torpedo motion is smaller than
356 the turbulence in this direction. At frequencies below f_a , $S\{u\}$ and $S\{v\}$ increase dramatically.
357 This suggests that unresolved, low-frequency motion of the torpedo is contaminating the velocity
358 measurements at these frequencies. It may be possible to correct for some of this contamination
359 using a measurement of the ship's motion as a proxy for the torpedo's low-frequency motion,
360 but this has not been done. Still, above f_a , the torpedo appears to provide a reliable estimate of
361 spectral amplitude in the inertial subrange and can therefore be used to estimate ε . Considering
362 the simplicity of the platform, it may be a useful option for quantifying this turbulence statistic in
363 a variety of scenarios. If a GPS is positioned above it, it may be capable of providing even more.

364 *e. Cross Spectra*

365 Cross-spectra indicate the correlation between different velocity components as a function of fre-
366 quency, and their integrals are the Reynold's stresses. Head motion cross-spectra, $C\{\mathbf{u}_h\}$ (Figure

367 12, red), and uncorrected velocity cross-spectra, $C\{\mathbf{u}_m\}$ (black), from TTM measurements have
368 large peaks at the same frequency (0.15 Hz) as peaks in auto-spectra (Figure 9). This indicates
369 that mooring motion contaminates the uncorrected cross-spectral velocity measurements, and that
370 Reynold's stress estimates based on uncorrected velocity measurements will be contaminated by
371 mooring motion.

372 Fortunately, motion corrected velocity cross-spectra, $C\{\mathbf{u}\}$ (Figure 12, blue), have reduced
373 cross-spectral amplitudes at these frequencies. This indicates that motion correction reduces mo-
374 tion contamination to produce more reliable estimates of velocity cross spectra and Reynold's
375 stresses (Figure 12). Notably, the low standard deviation of $fC\{\mathbf{u}\}$ (indicated by the blue shading)
376 compared to the mean values of $fC\{\mathbf{u}_h\}$ and $fC\{\mathbf{u}_m\}$ —at the frequencies of maximum motion—
377 indicates that even the individual values of $C\{\mathbf{u}\}$ are reduced at these frequencies, compared to
378 $C\{\mathbf{u}_m\}$, not just their mean.

379 These results indicate that motion-corrected TTM velocity measurements can be used to estimate
380 turbulence Reynold's stresses. Without motion correction, Reynold's stress estimates would be
381 contaminated by the large peaks in the cross spectra that are caused by the swaying and fluttering
382 motion of the TTM vane. Cross-spectra of TTM data for other velocity ranges (i.e., $< 2 \text{ ms}^{-1}$),
383 and cross-spectra from the SMB show similar results (not shown). However, we note that because
384 the SMB is less-stable in pitch than the TTM (see Part I for details), the TTM provides a more
385 accurate estimates of \bar{uw} .

386 In order to compare the cross-spectra to other measurements, we normalize them following
387 Kaimal et al. (1972) as: $\hat{C}\{u, w\}(\hat{f}) = -C\{u, w\}f_o/u_*^2$, where $f_o = \bar{U}/z$ and $\hat{f} = f/f_o$. When
388 plotted on a log-log scale, $\hat{C}\{u, w\}$ has a $\hat{f}^{-7/3}$ high-frequency spectral slope that is consistent
389 with other measurements (Figure 13). At low-frequency, the cross-spectra are more than 10x
390 smaller than the semi-empirical Kaimal form, but this discrepancy is consistent with other mea-

surements of cross-spectra. In particular, Walter et al. (2011) observed a half-decade reduction from the Kaimal form near the seafloor, and measurements from an ADV positioned 4.6 m above the seafloor on a fixed tripod at a different site in Puget Sound show a similar degree of deviation as observed here (Thomson et al. 2012).

While one might be inclined to attribute the discrepancy between these estimates and the Kaimal form to normalization by local u_* , the agreement between auto-spectra and their Kaimal form suggests otherwise (Figure 9). Instead, we conclude that either the Kaimal cross-spectra do not apply universally at distances far from the bottom boundary, or the spectra are being modified by physics other than bottom boundary layer driven turbulence. Either way, the agreement of TTM-measured cross-spectra with measurements from stationary platforms is interpreted as an indication that this platform can resolve cross-spectra and Reynold's stresses.

5. Discussion

Ideally, moored motion-corrected turbulence velocity measurements would be validated against simultaneous independent validated measurements of turbulence velocity at the same scales, time, and location. Accomplishing this, however, involves significant technical challenges that are not easily overcome—most notably the difficulty of measuring turbulence at the same point as the moving ADV. A slightly less ideal but much more realistic confirmation of the methodology might involve comparing the statistics of moored turbulence measurements to those from a nearby fixed platform, or a fixed platform placed at the same location at a different time (e.g., the “tripod” platform described in Thomson et al. 2012). Unfortunately, to our knowledge, these measurements have not yet been made.

The previous section showed that the shape of the turbulence velocity spectra from moored ADVs is consistent with Kolmogorov's theory of locally isotropic turbulence, which has been ob-

414 served consistently in turbulence measurements for decades (Kolmogorov 1941; Grant et al. 1962;
 415 McMillan et al. 2016). This is interpreted as the first indication that the measurement systems
 416 presented are capable of accurately resolving turbulence. The degree to which uncorrected spec-
 417 tra were corrected toward this theoretical and observationally confirmed shape is interpreted as a
 418 measure of the improvement of the spectral estimates by motion correction. This section takes
 419 that reasoning one step further to demonstrate that motion-corrected velocity measurements can
 420 produce estimates of turbulence statistics that are consistent with the physical processes that can
 421 be reasonably assumed to dominate the measurement site.

422 Figure 14 presents a time series of the mean velocity (A) and several turbulence statistics that
 423 were measured during the June 2014 TTM deployment. This figure shows the evolution of the flow
 424 through Admiralty Inlet during 1.5 tidal cycles. The tke (B), Reynold's stresses (C), dissipation,
 425 and one component of turbulence production (D) grow and strengthen with ebb or flood then
 426 subside during slack tide. This component of turbulence production is:

$$P_{uz} = \bar{uw} \frac{\partial \bar{u}}{\partial z} . \quad (4)$$

427 Where $\partial \bar{u} / \partial z$ is computed from the two ADVs on the TTM. The highest values of ε and P_{uz} occur
 428 at the peak of the ebb or flood, which is in agreement with other measurements in tidal channels.
 429 The agreement of the magnitude of P_{uz} with ε at those times suggests a local production-dissipation
 430 balance that is often observed in tidally forced channels (Trowbridge et al. 1999; Stacey et al.
 431 1999b; McMillan et al. 2016). At other times, the value of P_{uz} is insufficient to balance ε or is
 432 negative.

433 Inspection of the negative P_{uz} values reveals that most of them are caused by a reversed sign of \bar{uw}
 434 rather than a reversed sign of $\partial u / \partial z$ (i.e., when compared to the sign of u). This finding suggests
 435 that uncertainty in \bar{uw} may be contributing to discrepancies between P_{uz} and ε . Furthermore,

436 considering the complex nature of the bathymetry and shoreline at this site (i.e., the headland), it
437 is not surprising that P_{uz} does not perfectly balance ε . Other terms of the tke equation are likely
438 to be important, such as turbulence advection, other components of production, and turbulent
439 transport. The fact that P_{uz} and ε are in near balance as often as they are indicates that bottom
440 boundary layer physics are important to the turbulence dynamics at this site.

441 Given the assumptions implicit in this comparison and the discussion above, agreement between
442 P_{uz} and ε —especially for the highest values of ε —suggests the turbulent boundary layer reaches
443 the depth of these measurements (10 m) during the highest flow speeds (Figure 15). This result
444 is further supported by a comparison of \bar{U} with ε (Figure 16). Here we see a $\varepsilon \propto \bar{U}^3$ dependence
445 that is again suggestive of bottom boundary layer physics (Trowbridge 1992; Nash et al. 2009). At
446 lower flow speeds, ε deviates from this relationship, which suggests that the boundary layer is no
447 longer the dominant physical process at the depth of these measurements.

448 There are two intriguing differences between the ebb and flood datasets: 1) the drag coefficient
449 relating ε to \bar{U}^3 is larger for ebbs, and 2) the fit does not hold as well for low flow speeds (Figure
450 16). These details are not surprising considering the complex bathymetry at the test site (Figure
451 1). In particular, the flow immediately upstream of the measurement site is exposed to much
452 more bathymetric curvature—i.e. from the headland—during ebb (when \bar{u} is > 0) than the during
453 flood ($\bar{u} < 0$). Based on this, one might expect flow separation (turbulence advection), turbulence
454 production, or turbulence transport emanating from the headland to have a stronger impact on
455 the flow at this site during ebb than flood. These effects are a likely contributor to the distinct
456 relationships observed in Figure 16.

457 The hypothesis that the headland is a key contributor to the turbulence dynamics at this site
458 suggests that terms such as cross-stream turbulence advection, $\bar{v}\partial\text{tke}/\partial y$, the lateral turbulent
459 transport terms, $\partial\bar{u}_i\bar{u}_i\bar{v}/\partial y$, or lateral shear production, $\bar{u}\bar{v}\partial\bar{u}/\partial y$, may contribute significantly to

the dynamics of turbulence at this site. While we did not measure stratification profiles during these measurements, we do not typically expect buoyancy flux to play a dominant role due to the fact that this region tends to be tidally well-mixed (Geyer and Cannon 1982). In summary, bottom boundary layer physics seems to be the dominant process at the measurement site, with lateral advection, lateral transport, and lateral production of tke also potentially contributing—especially during ebb. A more detailed analysis of the turbulence and momentum dynamics of this headland is left for future work (e.g., similar to Warner et al. 2013).

6. Conclusion

This work presents a methodology for measuring turbulence from moored ADV-IMUs and demonstrates that motion correction reduces mooring motion-contamination. Comparison of spectra of ADV head motion, $S\{\mathbf{u}_h\}$, to that of motion-corrected, $S\{\mathbf{u}\}$, and uncorrected spectra, $S\{\mathbf{u}_m\}$, reveals that motion correction improves spectral estimates of moored ADV measurements. In particular, we found that motion-corrected spectra have spectral shapes that are similar to previous measurements of tidal-channel turbulence and have $f^{-5/3}$ spectral slopes at high frequencies. This finding suggests that the motion-corrected spectra resolve the inertial subrange predicted by Kolmogorov’s theory of locally isotropic turbulence.

Motion correction reduces motion contamination for all platforms we presented but it does not necessarily remove it completely. This outcome seems to depend on the relative amplitude of platform motion compared to the underlying turbulence being measured. The most notable example of this is from TTM $S\{v\}$, which have large-amplitude “swaying” peaks at 0.15 Hz that interrupts the frequently observed ‘roll-off’ between the low-frequency ‘energy containing scales’ and the $f^{-5/3}$ inertial subrange.

482 The possibility of persistent motion contamination requires that turbulence measurements from
483 moored, motion-corrected ADV-IMUs be interpreted with care. An inspection of spectra presented
484 here suggests that excluding spectral regions where $S\{\mathbf{u}_h\}/S\{\mathbf{u}\} > 3$ removes persistent-motion
485 contamination peaks while still preserving spectral regions where motion correction is effective.
486 Using this criteria, it is then possible to produce spectral fits that exclude persistent-motion con-
487 tamination, and provide reliable estimates of turbulence quantities of interest (e.g., ε and tke).

488 We have also shown that motion correction reduces motion contamination in cross spectra. This
489 finding is important because it suggests that moored ADV-IMU measurements may be used to
490 produce reliable estimates of Reynolds stresses. We utilized these stress estimates and vertical
491 shear estimates, both from the TTM, to estimate P_{uz} .

492 Finally, we have shown that ε estimates based on motion-corrected spectra scale with \bar{U}^3 , and
493 balance P_{uz} estimates during peak ebb and flood. Together, these results indicate that bottom
494 boundary layer physics are a dominant process at this site, and that the boundary layer reaches the
495 height of the ADV-IMUs (10 m) during ebb and flood. The degree of agreement between P_{uz} and ε
496 also serves as an indicator of the self-consistency of moored ADV-IMU turbulence measurements.

497 *Acknowledgments.* Many thanks to Joe Talbert, Alex DeKlerk, Captain Andy Reay-Ellers, Jen-
498 nifer Rinker, Maricarmen Guerra, and Eric Nelson in assisting with data collection. The authors
499 are also grateful to James VanZwieten, Matthew Egeland and Marshall Richmond for discussion
500 on the details of this work.

501 Thanks to the open-source software community for the tools used in this work, especially the
502 developers of LATEX, Python, NumPy, Matplotlib, git, and GNU emacs.

503 This work was supported by the U.S. Department of Energy under Contract No. DE-AC36-
504 08GO28308 with the National Renewable Energy Laboratory. Funding for the work was provided

505 by the DOE Office of Energy Efficiency and Renewable Energy, Wind and Water Power Technolo-
506 gies Office.

507 The U.S. Government retains and the publisher, by accepting the article for publication, ac-
508 knowledges that the U.S. Government retains a nonexclusive, paid-up, irrevocable, worldwide
509 license to publish or reproduce the published form of this work, or allow others to do so, for U.S.
510 Government purposes.

511 **References**

- 512 Afgan, I., J. McNaughton, S. Rolfo, D. Apsley, T. Stallard, and P. Stansby, 2013: Turbulent flow
513 and loading on a tidal stream turbine by les and rans. *International Journal of Heat and Fluid*
514 *Flow*, **43**, 96–108.
- 515 Alexander, S. R., and P. E. Hamlington, 2015: Analysis of turbulent bending moments in tidal
516 current boundary layers. *Journal of Renewable and Sustainable Energy*, **7 (6)**, 063 118.
- 517 Alford, M. H., 2010: Sustained, full-water-column observations of internal waves and mixing near
518 mendocino escarpment. *Journal of Physical Oceanography*, **40 (12)**, 2643–2660, doi:10.1175/
519 2010JPO4502.1.
- 520 Axford, D., 1968: On the accuracy of wind measurements using an inertial platform in an aircraft,
521 and an example of a measurement of the vertical mesostructure of the atmosphere. *Journal of
522 Applied Meteorology*, **7 (4)**, 645–666.
- 523 Barshan, B., and H. F. Durrant-Whyte, 1995: Inertial navigation systems for mobile robots. *IEEE
524 Transactions on Robotics and Automation*, **11 (3)**, 328–342.
- 525 Bevly, D. M., 2004: Global positioning system (gps): A low-cost velocity sensor for correcting in-
526 erial sensor errors on ground vehicles. *Journal of dynamic systems, measurement, and control*,
527 **126 (2)**, 255–264.
- 528 Cartwright, G. M., C. T. Friedrichs, P. J. Dickhudt, T. Gass, and F. H. Farmer, 2009: Using the
529 acoustic doppler velocimeter (adv) in the mudbed real-time observing system. *Marine Technol-
530 ogy for Our Future: Global and Local Challenges*.
- 531 Doherty, K., D. Frye, S. Liberatore, and J. Toole, 1999: A moored profiling instrument*. *Journal
532 of Atmospheric and Oceanic Technology*, **16 (11)**, 1816–1829.

- 533 Edson, J. B., A. A. Hinton, K. E. Prada, J. E. Hare, and C. W. Fairall, 1998: Direct covariance
534 flux estimates from mobile platforms at sea*. *Journal of Atmospheric and Oceanic Technology*,
535 **15** (2), 547–562, doi:10.1175/1520-0426(1998)015<0547:DCFEFM>2.0.CO;2.
- 536 Egeland, M. N., 2014: Spectral evaluation of motion compensated ADV systems for ocean turbu-
537 lence measurements. Ph.D. thesis, Florida Atlantic University.
- 538 Fer, I., and M. B. Paskyabi, 2014: Autonomous ocean turbulence measurements using shear probes
539 on a moored instrument. *Journal of Atmospheric and Oceanic Technology*, **31** (2), 474–490, doi:
540 10.1175/JTECH-D-13-00096.1.
- 541 Finlayson, D., 2005: Combined bathymetry and topography of the Puget Lowlands,
542 Washington state. URL <https://www.ocean.washington.edu/data/pugetsound/psdem2005.html>,
543 g1230485.zip, retrieved September 2014.
- 544 Geyer, R. W., M. E. Scully, and D. K. Ralston, 2008: Quantifying vertical mixing in estuaries.
545 *Environmental Fluid Mechanics*, **8**, 495–509, doi:10.1007/s10652-008-9107-2.
- 546 Geyer, W. R., and G. A. Cannon, 1982: Sill processes related to deep water renewal in a fjord. *Jour-*
547 *nal of Geophysical Research: Oceans*, **87** (C10), 7985–7996, doi:10.1029/JC087iC10p07985.
- 548 Goodman, L., E. R. Levine, and R. G. Lueck, 2006: On measuring the terms of the turbulent
549 kinetic energy budget from an auv. *Journal of Atmospheric and Oceanic Technology*, **23** (7),
550 977–990, doi:10.1175/JTECH1889.1.
- 551 Grant, H. L., R. W. Stewart, and A. Moilliet, 1962: Turbulence spectra from a tidal channel.
552 *Journal of Fluid Mechanics*, **12**, 241–263.
- 553 Guerra Paris, M., and J. Thomson, 2017: Turbulence measurements from 5-beam acoustic doppler
554 current profilers. *Journal of Atmospheric and Oceanic Technology*.

- 555 Gulmammadov, F., 2009: Analysis, modeling and compensation of bias drift in mems inertial
556 sensors. *Recent Advances in Space Technologies, 2009. RAST'09. 4th International Conference*
557 on, IEEE, 591–596.
- 558 Gunawan, B., V. S. Neary, and J. Colby, 2014: Tidal energy site resource assessment in the East
559 River tidal strait, near Roosevelt Island, New York, NY (USA). *Renewable Energy*, **71**, 509–
560 517, doi:10.1016/j.renene.2014.06.002.
- 561 Hand, M. M., N. D. Kelley, and M. J. Balas, 2003: Identification of wind turbine response to
562 turbulent inflow structures. Tech. Rep. NREL/CP-500-33465, National Renewable Energy Lab-
563 oratory.
- 564 Harding, S., L. Kilcher, and J. Thomson, 2017: Turbulence measurements from compliant moor-
565 ings - part 1: Motion characterization, in review.
- 566 Kaimal, J. C., J. C. Wyngaard, Y. Izumi, and O. R. Cote, 1972: Spectral characteristics of surface-
567 layer turbulence. *Quart. J. Roy. Meteor. Soc*, **98 (417)**, 563–689.
- 568 Kelley, N. D., B. J. Jonkman, G. N. Scott, J. T. Bialasiewicz, and L. S. Redmond, 2005: The impact
569 of coherent turbulence on wind turbine aeroelastic response and its simulation. *WindPower*,
570 Denver, Colorado, NREL/CP-500-38074, may 15-18.
- 571 Kilcher, L., J. Thomson, and S. Harding, 2017: Admiralty inlet advanced turbulence measure-
572 ments: final data and code archive [data set]. URL <http://mhkdir.openei.org/submissions/223>,
573 created 05-31-2017.
- 574 Kilcher, L., J. Thomson, J. Talbert, and A. DeKlerk, 2016: Measuring turbulence from moored
575 acoustic Doppler velocimeters: A manual to quantifying inflow at tidal energy sites. 9 62979,
576 National Renewable Energy Laboratory. URL www.nrel.gov/docs/fy16osti/62979.pdf.

- 577 Kim, S. C., C. T. Friedrichs, J. P.-Y. Maa, and L. D. Wright, 2000: Estimating bottom stress in
578 tidal boundary layer from acoustic doppler velocimeter data. *Journal of Hydraulic Engineering*,
579 399–406.
- 580 Kolmogorov, A. N., 1941: Dissipation of energy in the locally isotropic turbulence. *Dokl. Akad.*
581 *Nauk SSSR*, **32** (1), 16–18, URL <http://www.jstor.org/stable/51981>.
- 582 Kraus, N. C., A. Lohrmann, and R. Cabrera, 1994: A new acoustic meter for measuring 3D
583 laboratory flows. *Journal of Hydraulic Engineering*, **120**, 406–412.
- 584 Lohrmann, A., R. Cabrera, G. Gelfenbaum, and J. Haines, 1995: Direct measurements of reynolds
585 stress with an acoustic doppler velocimeter. *Current Measurement, 1995.*, *Proceedings of the*
586 *IEEE Fifth Working Conference on*, 205–210, doi:10.1109/CCM.1995.516175.
- 587 Lorke, A., 2007: Boundary mixing in the thermocline of a large lake. *Journal of Geophysical*
588 *Research: Oceans*, **112** (C9), n/a–n/a, doi:10.1029/2006JC004008, c09019.
- 589 Lueck, R. G., and D. Huang, 1999: Dissipation measurement with a moored instrument in a swift
590 tidal channel. *Journal of atmospheric and oceanic technology*, **16**, 1499–1505.
- 591 Lumley, J., and E. Terray, 1983: Kinematics of turbulence convected by a random wave field.
592 *Journal of Physical Oceanography*, **13** (11), 2000–2007.
- 593 McCaffrey, K., B. Fox-Kemper, P. E. Hamlington, and J. Thomson, 2015: Characterization of
594 turbulence anisotropy, coherence, and intermittency at a prospective tidal energy site: Observa-
595 tional data analysis. *Renewable Energy*, **76**, 441–453.
- 596 McMillan, J. M., A. E. Hay, R. G. Lueck, and F. Wolk, 2016: Rates of dissipation of turbulent
597 kinetic energy in a high reynolds number tidal channel. *Journal of Atmospheric and Oceanic*
598 *Technology*, **33** (4), 817–837, doi:10.1175/JTECH-D-15-0167.1.

- 599 MicroStrain, I., 2010: Technical note: Coning and sculling. Tech. Rep. I0019, MicroStrain. URL
600 http://files.microstrain.com/TN-I0019_3DM-GX3-25__Coning_And_Sculling.pdf.
- 601 MicroStrain, I., 2012: *3DM-GX3-15,-25 MIP Data Communications Protocol*. URL <http://files.microstrain.com/3DM-GX3-15-25-MIP-Data-Communications-Protocol.pdf>, retrieved
602 January 2014.
- 603
- 604 Miller, S. D., T. S. Hristov, J. B. Edson, and C. A. Friehe, 2008: Platform motion effects on
605 measurements of turbulence and air-sea exchange over the open ocean. *Journal of Atmospheric*
606 and *Oceanic Technology*, **25** (9), 1683–1694, doi:10.1175/2008JTECHO547.1.
- 607 Morison, J. R., J. W. Johnson, and S. A. Schaaf, 1950: The force exerted by surface waves on
608 piles. *Journal of Petroleum Technology*, **2** (05), 149–154.
- 609 Moum, J., and J. Nash, 2009: Mixing measurements on an equatorial ocean mooring. *Journal of*
610 *Atmospheric and Oceanic Technology*, **26** (2), 317–336.
- 611 Mücke, T., D. Kleinhans, and J. Peinke, 2011: Atmospheric turbulence and its influence on the
612 alternating loads on wind turbines. *Wind Energy*, **14**, 301–316.
- 613 Nash, J. D., L. F. Kilcher, and J. N. Moum, 2009: Structure and composition of a strongly
614 stratified, tidally pulsed river plume. *Journal of Geophysical Research*, **114**, C00B12, doi:
615 10.1029/2008JC005036.
- 616 Nash, J. D., E. Kunze, J. M. Toole, and R. W. Schmitt, 2004: Internal tide reflection and turbulent
617 mixing on the continental slope. *Journal of Physical Oceanography*, **34** (5), 1117–1134, doi:
618 10.1175/1520-0485(2004)034<1117:ITRATM>2.0.CO;2.
- 619 Nortek, 2005: *Vector Current Meter User Manual*. Vangkroken 2, NO-1351 RUD, Norway, h ed.

- 620 Paskyabi, M. B., and I. Fer, 2013: Turbulence measurements in shallow water from a subsurface
621 moored moving platform. *Energy Procedia*, **35**, 307 – 316, doi:10.1016/j.egypro.2013.07.183.
- 622 Perlin, A., and J. N. Moum, 2012: Comparison of thermal variance dissipation rates from moored
623 and profiling instruments at the equator. *Journal of Atmospheric and Oceanic Technology*.
- 624 Polagye, B., and J. Thomson, 2013: Tidal energy resource characterization: methodology and field
625 study in admiralty inlet, Puget Sound, WA (USA). *Proceedings of the Institution of Mechanical
626 Engineers, Part A: Journal of Power and Energy*, **227** (3), 352–367.
- 627 Rippeth, T. P., E. Williams, and J. H. Simpson, 2002: Reynolds stress and turbulent en-
628 ergy production in a tidal channel. *Journal of Physical Oceanography*, **32**, 1242–1251, doi:
629 10.1175/1520-0485(2002)032\$1242:RSATEP\$2.0.CO;2.
- 630 Sreenivasan, K. R., 1995: On the universality of the Kolmogorov constant. *Physics of Fluids*, **7**,
631 2778–2784.
- 632 Stacey, M. T., S. G. Monismith, and J. R. Burau, 1999a: Measurements of reynolds stress
633 profiles in unstratified tidal flow. *J. Geophys. Res.*, **104** (C5), 10 933–10 949, doi:10.1029/
634 1998JC900095.
- 635 Stacey, M. T., S. G. Monismith, and J. R. Burau, 1999b: Observations of turbulence in a partially
636 stratified estuary. *Journal of Physical Oceanography*, **29**, 1950–1970.
- 637 Thomson, J., B. Polagye, V. Durgesh, and M. Richmond, 2012: Measurements of turbulence at
638 two tidal energy sites in Puget Sound, WA. *Journal of Oceanic Engineering*, **37** (3), 363–374,
639 doi:10.1109/JOE.2012.2191656.
- 640 Trowbridge, J. H., 1992: A simple description of the deepening and structure of a stably stratified
641 flow driven by a surface stress. *Journal of Geophysical Research*, **97**, 15 529–15 543.

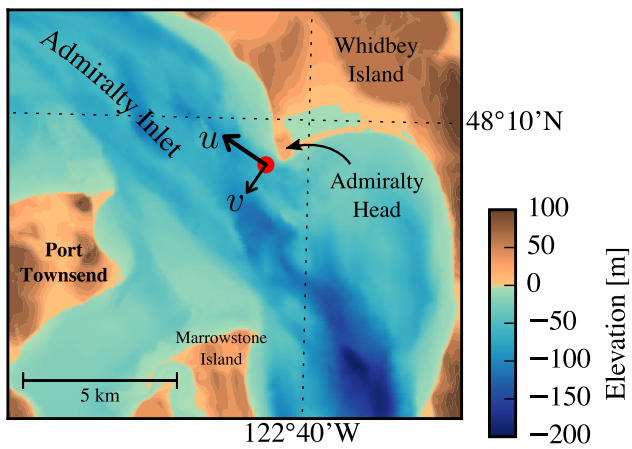
- 642 Trowbridge, J. H., W. R. Geyer, M. M. Bowen, and A. J. I. Williams, 1999: Near-bottom turbulence measurements in a partially mixed estuary: turbulent energy balance, velocity structure
643 and along-channel momentum balance. *Journal of Physical Oceanography*, **29**, 3056–3072.
- 644
- 645 van der Walt, S., S. C. Colbert, and G. Varoquaux, 2011: The numpy array: A structure for efficient
646 numerical computation. *Computing in Science & Engineering*, **13**, 22–30, doi:10.1109/MCSE.
647 2011.37.
- 648 VanZwieten, J. H., M. N. Egeland, K. D. von Ellenrieder, J. W. Lovenbury, and L. Kilcher, 2015:
649 Experimental evaluation of motion compensated adv measurements for in-stream hydrokinetic
650 applications. *Current, Waves and Turbulence Measurement (CWTM), 2015 IEEE/OES Eleventh*,
651 1–8, doi:10.1109/CWTM.2015.7098119.
- 652 Voulgaris, G., and J. H. Trowbridge, 1998: Evaluation of the acoustic doppler velocimeter (adv)
653 for turbulence measurements. *Journal of Atmospheric and Oceanic technology*, **15**, 272–289.
- 654 Walter, R. K., N. J. Nidzieko, and S. G. Monismith, 2011: Similarity scaling of turbulence spectra
655 and cospectra in a shallow tidal flow. *Journal of Geophysical Research: Oceans*, **116 (C10)**.
- 656 Warner, S. J., P. MacCready, J. N. Moum, and J. D. Nash, 2013: Measurement of tidal form drag
657 using seafloor pressure sensors. *Journal of Physical Oceanography*, **43 (6)**, 1150–1172.
- 658 Wiles, P. J., T. P. Rippeth, J. H. Simpson, and P. J. Hendricks, 2006: A novel technique for
659 measuring the rate of turbulent dissipation in the marine environment. *Geophysical Research
660 Letters*, **33**, 21 608.
- 661 Winkel, D., M. Gregg, and T. Sanford, 1996: Resolving oceanic shear and velocity with the multi-
662 scale profiler. *Journal of Atmospheric and Oceanic Technology*, **13 (5)**, 1046–1072.

- 663 Wyngaard, J. C., L. Rockwell, and C. A. Friehe, 1985: Errors in the measurement of turbulence
664 upstream of an axisymmetric body. *Journal of Atmospheric and Oceanic Technology*, **2** (4),
665 605–614.
- 666 Zhang, Y., K. Streitlien, J. G. Bellingham, and A. B. Baggeroer, 2001: Acoustic doppler ve-
667 locimeter flow measurement from an autonomous underwater vehicle with applications to deep
668 ocean convection. *Journal of Atmospheric and Oceanic Technology*, **18** (12), 2038–2051, doi:
669 [10.1175/1520-0426\(2001\)018<2038:ADVFMF>2.0.CO;2](https://doi.org/10.1175/1520-0426(2001)018<2038:ADVFMF>2.0.CO;2).

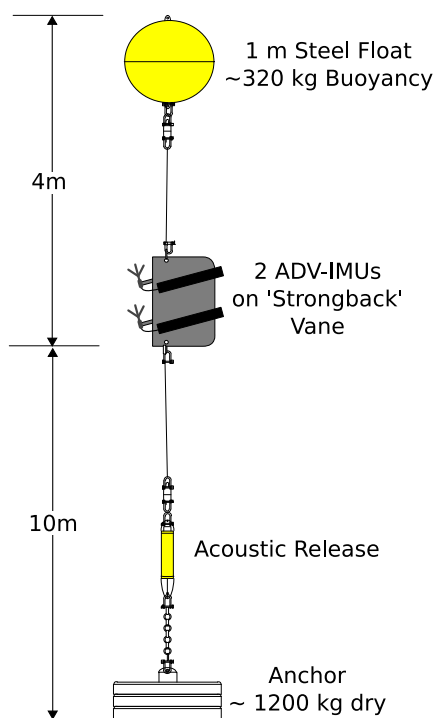
670 LIST OF FIGURES

671	Fig. 1. Bathymetry of Admiralty Inlet near Port Townsend, Washington, U.S.A. (Finlayson 2005). The red dot indicates the location of all measurements. The positive u direction is the direction of ebb flow (thick arrow originating from red dot), and positive v is away from Admiralty Head (smaller arrow).	35
672		
673		
674		
675	Fig. 2. Schematic diagram of the TTM; not to scale. A pop-up buoy for anchor recovery is not shown, for simplicity.	36
676		
677	Fig. 3. TTM components on the deck of the R/V Jack Robertson. The TTM includes two ADVs, with pressure cases mounted on opposite sides of the fin. The anchor stack includes a pop-up buoy for retrieval. The green arrow indicates the vector from the IMU to the ADV head (face of the transmit transducer).	37
678		
679		
680		
681	Fig. 4. Top: Alex DeKlerk checks to ensure that the SMB buoy is properly fastened to its anchor; the RDI workhorse ADP can be seen in the rear instrument bay. A bridle is draped across the top of the buoy for deployment and recovery, and a small marker buoy fastened to the tail is useful during recovery. Bottom: a close-up of the SMB buoy with the ADV head and the top of its pressure case. The green arrow indicates the vector from the IMU to the ADV head.	38
682		
683		
684		
685		
686		
687	Fig. 5. The turbulence platform showing details of the ADV head and pressure case configuration. The green arrow indicates the vector from the IMU to the ADV head. The head cable was taped out of the way beneath the sounding weight tail fins shortly after taking this photo.	39
688		
689		
690	Fig. 6. The spectral noise levels of rotational velocity ($S\{\mathbf{n}_\omega\}$, yellow) and translational velocity ($S\{\mathbf{n}_a\}$, black) estimated from an ADV-IMU resting motionless on a table. Solid and dashed lines indicate the horizontal and vertical components, respectively, of $S\{\mathbf{n}_a\}$ and $S\{\mathbf{u}_{low}\}$. The \mathbf{n}_a signals are unfiltered (black), and high-pass filtered at 0.03 Hz (blue) and 0.3 Hz (red); vertical dotted lines indicate the filter frequency. Green lines are an estimate of \mathbf{u}_{low} for the TTM. Grey horizontal lines indicate the horizontal (solid) and vertical (dashed) ADV noise levels. The shaded region indicates the range of $S\{u\}$ presented in the next section.	40
691		
692		
693		
694		
695		
696		
697	Fig. 7. Motion-corrected velocity spectra, $S\{\mathbf{u}\}$, for a range of high-pass filter frequencies: $f_a = 0.3$ Hz (thin red), 0.03 Hz (blue), and 0.003 Hz (thick black). The vertical dotted lines indicate the filter frequency. The thick grey line is $S\{\mathbf{u}_h\}$ for $f_a = 0.003$ Hz. The data are from the June 2014 TTM deployment when $2.0 < \bar{u} < 2.5 \text{ ms}^{-1}$.	41
698		
699		
700		
701	Fig. 8. Time series of tidal velocity in June 2012 at Admiralty Head from ADV-IMU measurements (black), and an ADP on the anchor (red). Note that the vertical scale on the three axes vary by an order of magnitude; the small ticks in A and B are equivalent to the ticks in C.	42
702		
703		
704	Fig. 9. Turbulence spectra from the June 2014 TTM deployment. Each column is for a range of streamwise velocity magnitudes (indicated at top, in m s^{-1}). The rows are for each component of velocity (indicated at far right). The uncorrected spectra are black, the corrected spectra are blue, and the spectra of ADV head motion is red (also indicated in the legend). The vertical red dotted line indicates f_a for estimating \mathbf{u}_h ; below this frequency $S\{\mathbf{u}_h\}$ is plotted as a dashed line. Diagonal black dotted lines indicate a $f^{-5/3}$ slope. The cyan line in the first and last rows indicates the semi-empirical Kaimal spectrum for the measured values of u_* and \bar{U} . The number of spectral ensembles, N , in each column is indicated in the top row.	43
705		
706		
707		
708		
709		
710		
711		
712		

713	Fig. 10. Turbulence spectra from the SMB. The axes layout and annotations are identical to Figure 714 9, except that $S\{\mathbf{u}_h\}$ is plotted as a solid line at all frequencies because it is measured at all 715 frequencies.	44
716	Fig. 11. Turbulence spectra from the turbulence torpedo during a 35-minute period when the mean 717 velocity was 1.3 ms^{-1} . Annotations and line colors are identical to Figure 9.	45
718	Fig. 12. Variance preserving cross-spectra between components of \mathbf{u} (blue), \mathbf{u}_h (red), and \mathbf{u}_m (black) 719 from the June 2014 TTM deployment. The upper row is $fC\{u, v\}$, the middle row is 720 $fC\{u, w\}$, and the bottom row is $fC\{v, w\}$ (also indicated at right). Note that these cross- 721 spectra are between components of a velocity vector (e.g., \mathbf{u}), not between different vectors 722 (i.e., not between \mathbf{u} and \mathbf{u}_m). N is the number of spectral ensembles in this average, i.e. 723 when $2 < u < 2.5 \text{ ms}^{-1}$. The light blue shading indicates one standard deviation of $fC\{\mathbf{u}\}$	46
724	Fig. 13. Non-dimensional cross-spectra of motion corrected velocity, $\hat{C}\{u, w\}$, on a log-log scale. 725 The average over $\Delta\hat{f} = 0.04$ bins is shown in blue, and single points are grey (negative values 726 not shown). The semi-empirical Kaimal et al. (1972) form is shown as a thick black line, 727 and the red dashed line indicates a $\hat{f}^{-7/3}$ slope. Cross-spectral estimates from measurements 728 from a fixed ‘tripod’ are in purple.	47
729	Fig. 14. Time series of mean velocities (A), turbulence energy and its components (B), Reynold’s 730 stresses (C), and turbulence dissipation rate (D) measured by the TTM during the June 731 2014 deployment. Shading indicates periods of ebb ($\bar{u} > 1.0 \text{ ms}^{-1}$, grey) and flood 732 ($\bar{u} < -1.0 \text{ ms}^{-1}$, lighter grey).	48
733	Fig. 15. P_{uz} vs. ε during the June 2014 TTM deployment for values of $ u > 1 \text{ m/s}$. Values of negative 734 production are indicated as open circles.	49
735	Fig. 16. A log-log plot of ε vs. \bar{U} for the June 2014 TTM (diamonds) and May 2015 SMB (dots) 736 deployments, during ebb (left) and flood (right). Black points are 5-minute averages. Green 737 dots are mean values within speed bins of 0.2 m s^{-1} width that have at least 10 points (50 738 minutes of data); their vertical bars are 95% bootstrap confidence intervals. The blue line 739 shows a \bar{U}^3 slope, wherein the proportionality constant (blue box) is calculated by taking 740 the log-space mean of ε/\bar{U}^3	50



741 FIG. 1. Bathymetry of Admiralty Inlet near Port Townsend, Washington, U.S.A. (Finlayson 2005). The red
 742 dot indicates the location of all measurements. The positive u direction is the direction of ebb flow (thick arrow
 743 originating from red dot), and positive v is away from Admiralty Head (smaller arrow).



744 FIG. 2. Schematic diagram of the TTM; not to scale. A pop-up buoy for anchor recovery is not shown, for
745 simplicity.



746 FIG. 3. TTM components on the deck of the R/V Jack Robertson. The TTM includes two ADVs, with
747 pressure cases mounted on opposite sides of the fin. The anchor stack includes a pop-up buoy for retrieval. The
748 green arrow indicates the vector from the IMU to the ADV head (face of the transmit transducer).



749 FIG. 4. Top: Alex DeKlerk checks to ensure that the SMB buoy is properly fastened to its anchor; the
 750 RDI workhorse ADP can be seen in the rear instrument bay. A bridle is draped across the top of the buoy for
 751 deployment and recovery, and a small marker buoy fastened to the tail is useful during recovery. Bottom: a
 752 close-up of the SMB buoy with the ADV head and the top of its pressure case. The green arrow indicates the
 753 vector from the IMU to the ADV head.



754 FIG. 5. The turbulence platform showing details of the ADV head and pressure case configuration. The green
755 arrow indicates the vector from the IMU to the ADV head. The head cable was taped out of the way beneath the
756 sounding weight tail fins shortly after taking this photo.

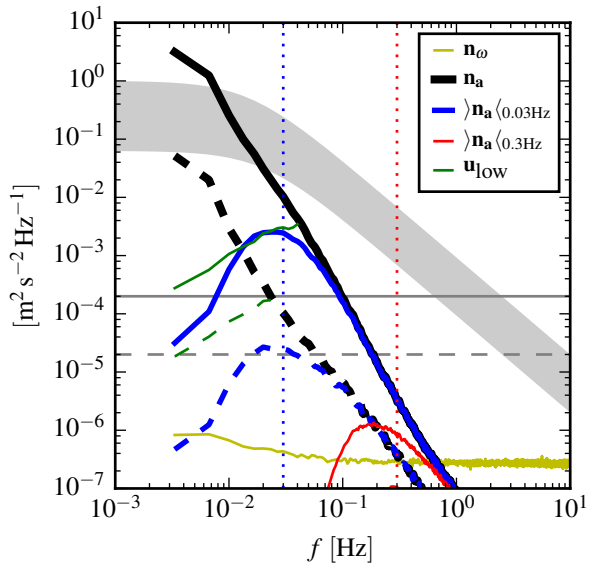
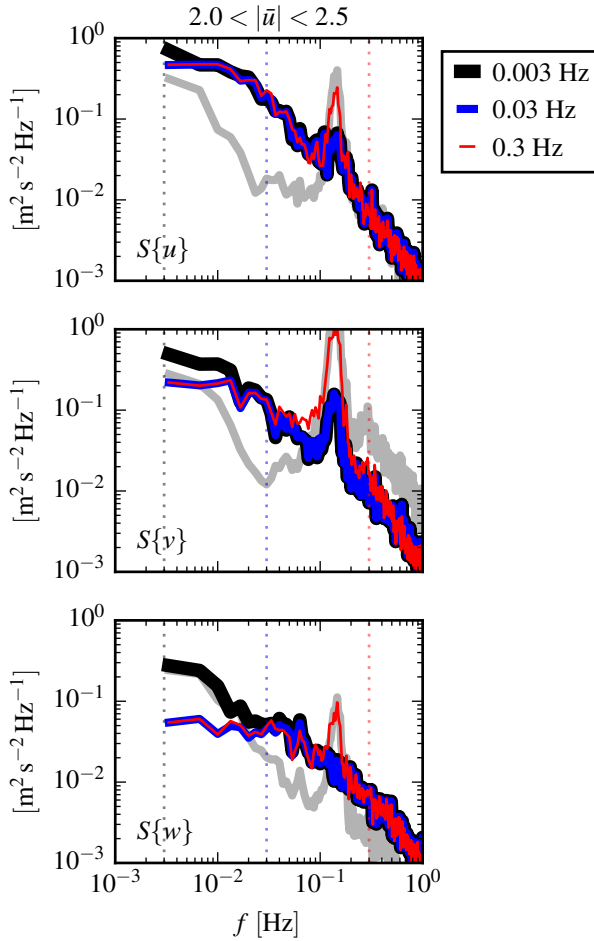
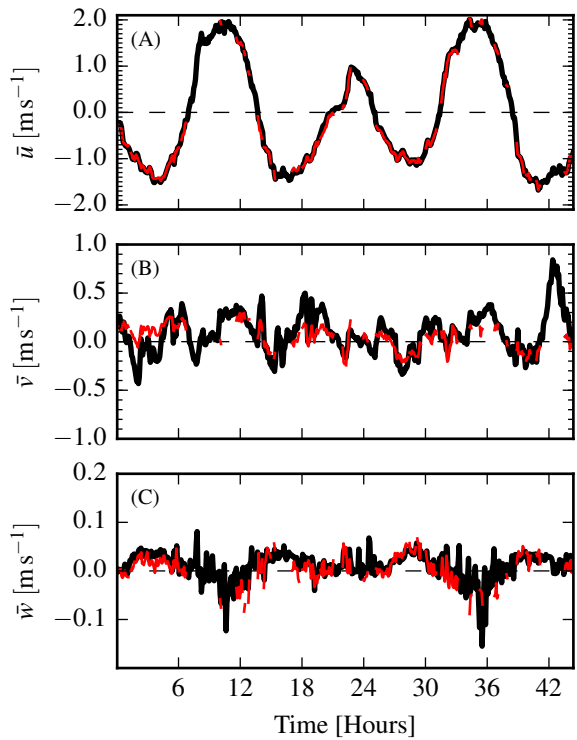


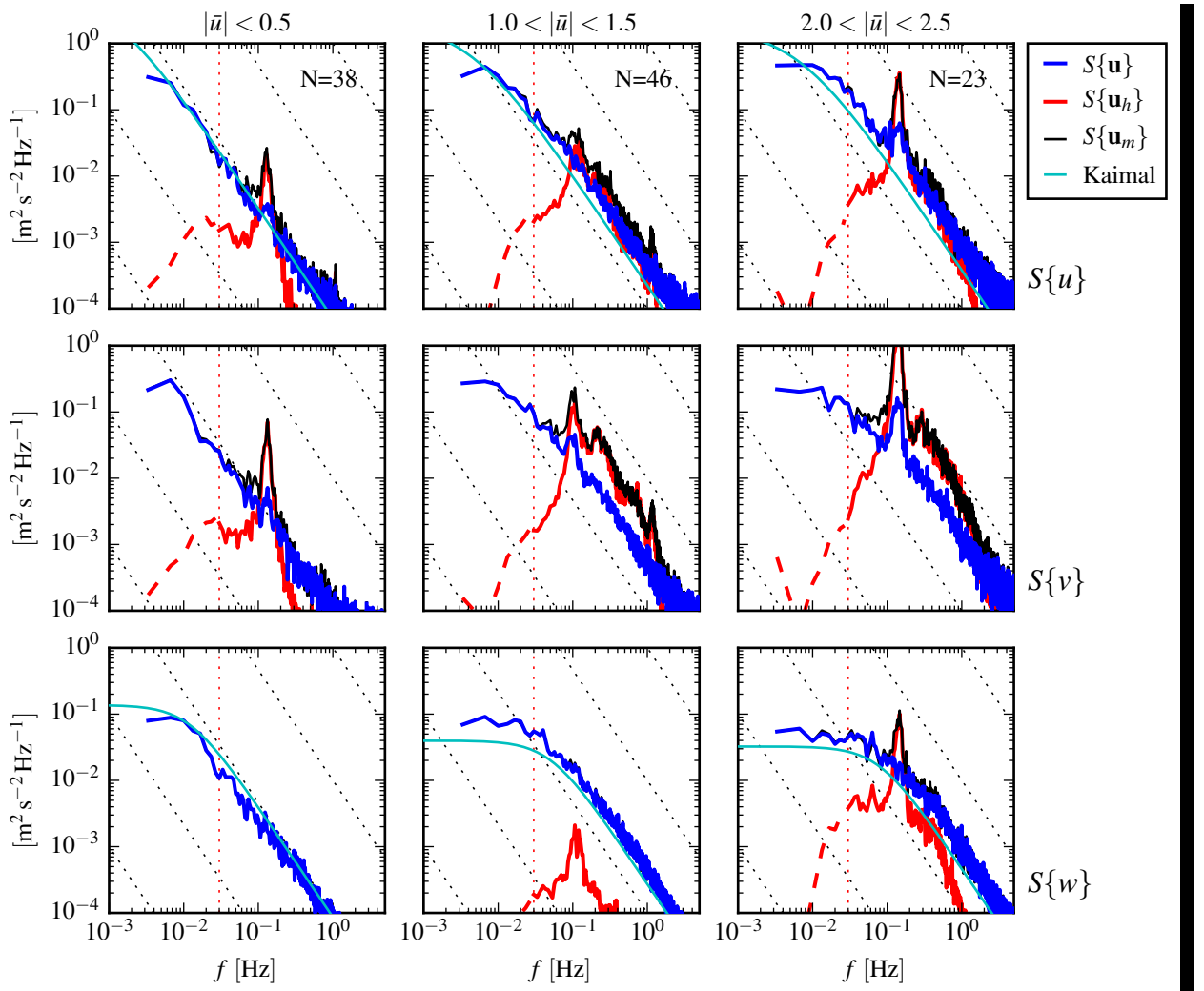
FIG. 6. The spectral noise levels of rotational velocity ($S\{n_\omega\}$, yellow) and translational velocity ($S\{n_a\}$, black) estimated from an ADV-IMU resting motionless on a table. Solid and dashed lines indicate the horizontal and vertical components, respectively, of $S\{n_a\}$ and $S\{u_{low}\}$. The n_a signals are unfiltered (black), and high-pass filtered at 0.03 Hz (blue) and 0.3 Hz (red); vertical dotted lines indicate the filter frequency. Green lines are an estimate of u_{low} for the TTM. Grey horizontal lines indicate the horizontal (solid) and vertical (dashed) ADV noise levels. The shaded region indicates the range of $S\{u\}$ presented in the next section.



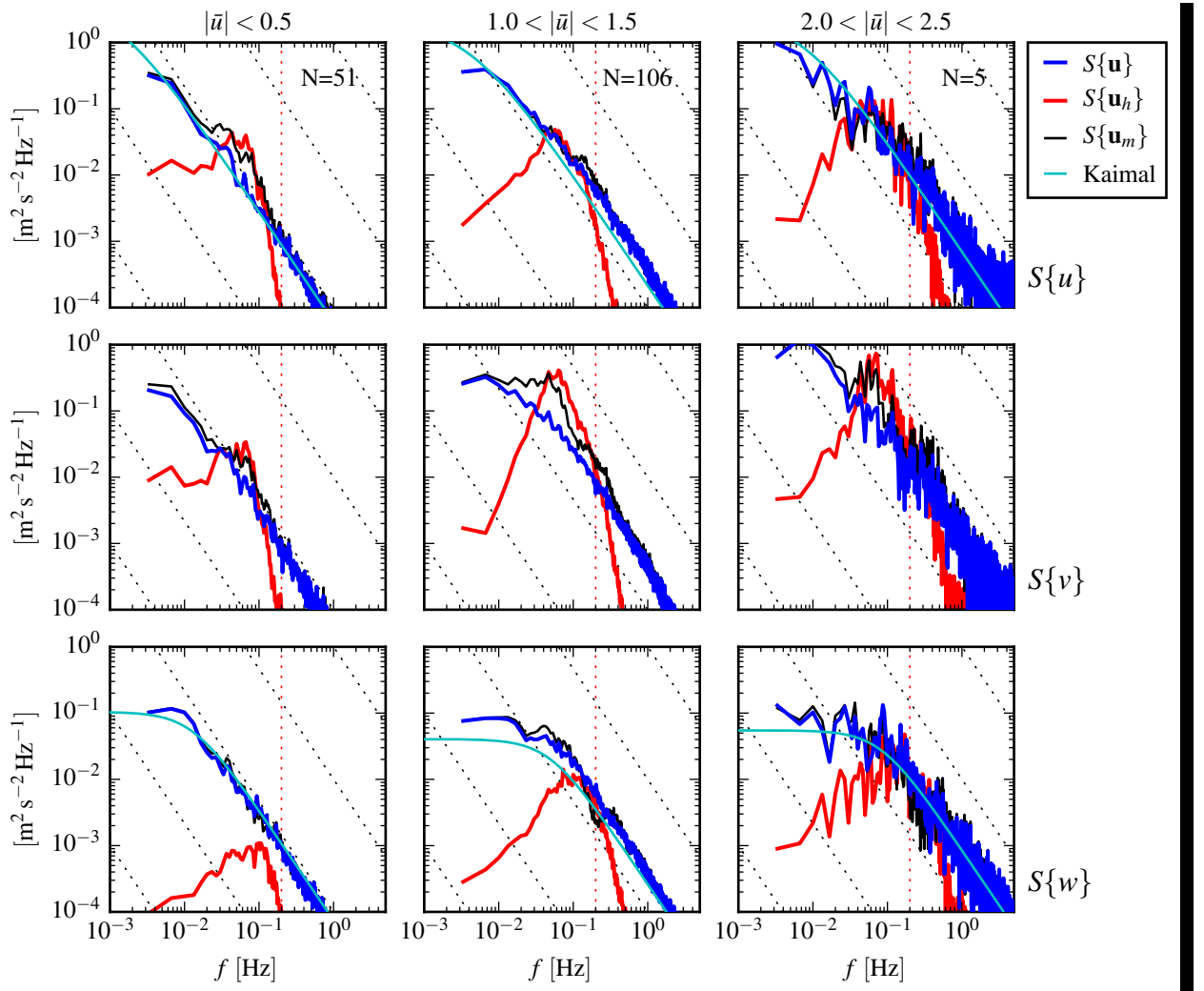
763 FIG. 7. Motion-corrected velocity spectra, $S\{\mathbf{u}\}$, for a range of high-pass filter frequencies: $f_a = 0.3$ Hz
 764 (thin red), 0.03 Hz (blue), and 0.003 Hz (thick black). The vertical dotted lines indicate the filter frequency.
 765 The thick grey line is $S\{\mathbf{u}_h\}$ for $f_a = 0.003$ Hz. The data are from the June 2014 TTM deployment when
 766 $2.0 < |\bar{u}| < 2.5 \text{ ms}^{-1}$.



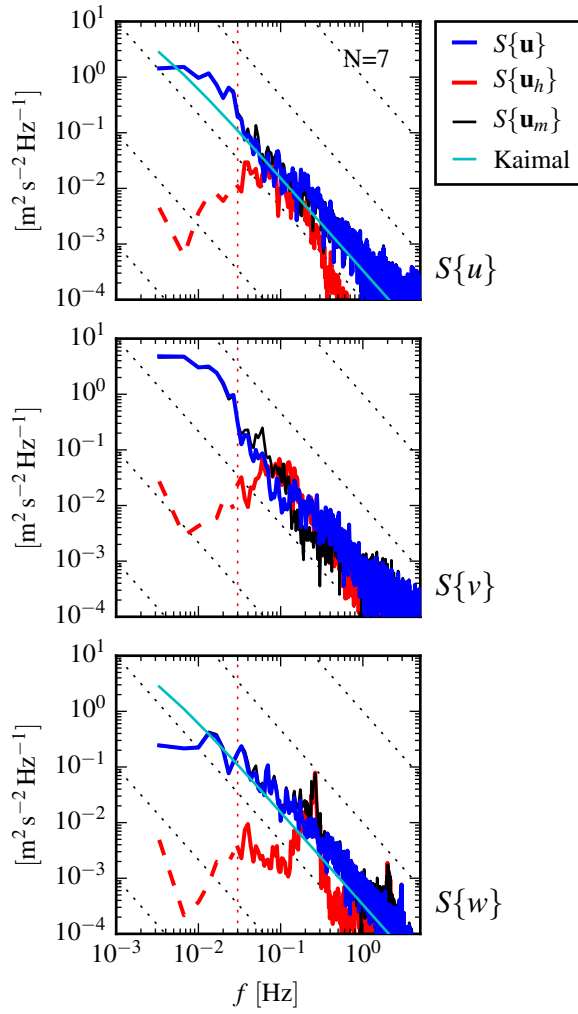
767 FIG. 8. Time series of tidal velocity in June 2012 at Admiralty Head from ADV-IMU measurements (black),
 768 and an ADP on the anchor (red). Note that the vertical scale on the three axes vary by an order of magnitude;
 769 the small ticks in A and B are equivalent to the ticks in C.



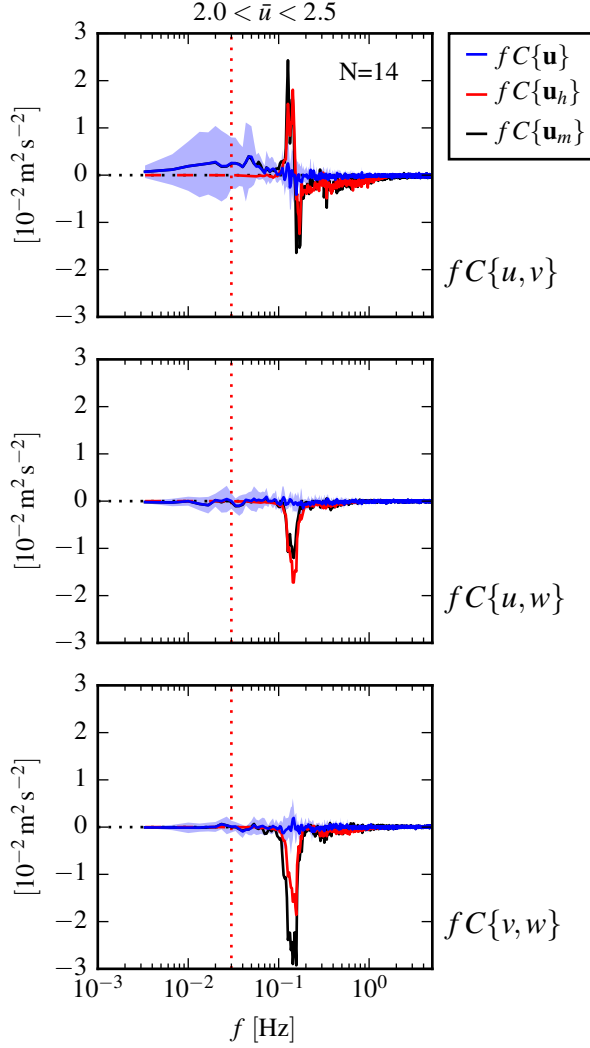
770 FIG. 9. Turbulence spectra from the June 2014 TTM deployment. Each column is for a range of streamwise
 771 velocity magnitudes (indicated at top, in m s^{-1}). The rows are for each component of velocity (indicated at far
 772 right). The uncorrected spectra are black, the corrected spectra are blue, and the spectra of ADV head motion is
 773 red (also indicated in the legend). The vertical red dotted line indicates f_a for estimating \mathbf{u}_h ; below this frequency
 774 $S\{\mathbf{u}_h\}$ is plotted as a dashed line. Diagonal black dotted lines indicate a $f^{-5/3}$ slope. The cyan line in the first
 775 and last rows indicates the semi-empirical Kaimal spectrum for the measured values of u_* and \bar{U} . The number
 776 of spectral ensembles, N, in each column is indicated in the top row.



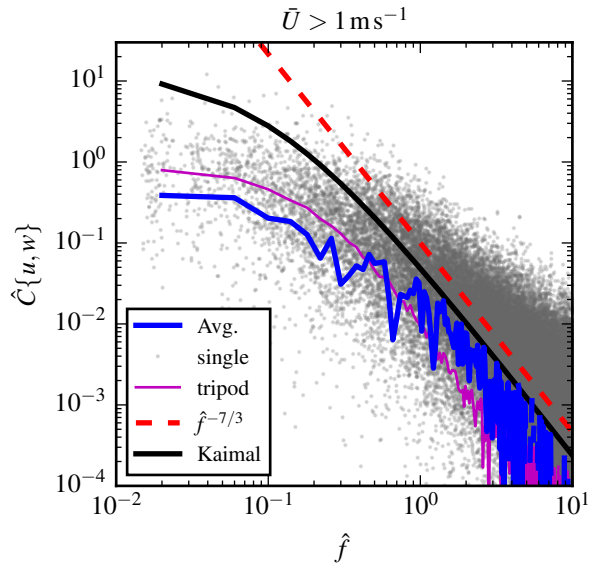
777 FIG. 10. Turbulence spectra from the SMB. The axes layout and annotations are identical to Figure 9, except
 778 that $S\{\mathbf{u}_h\}$ is plotted as a solid line at all frequencies because it is measured at all frequencies.



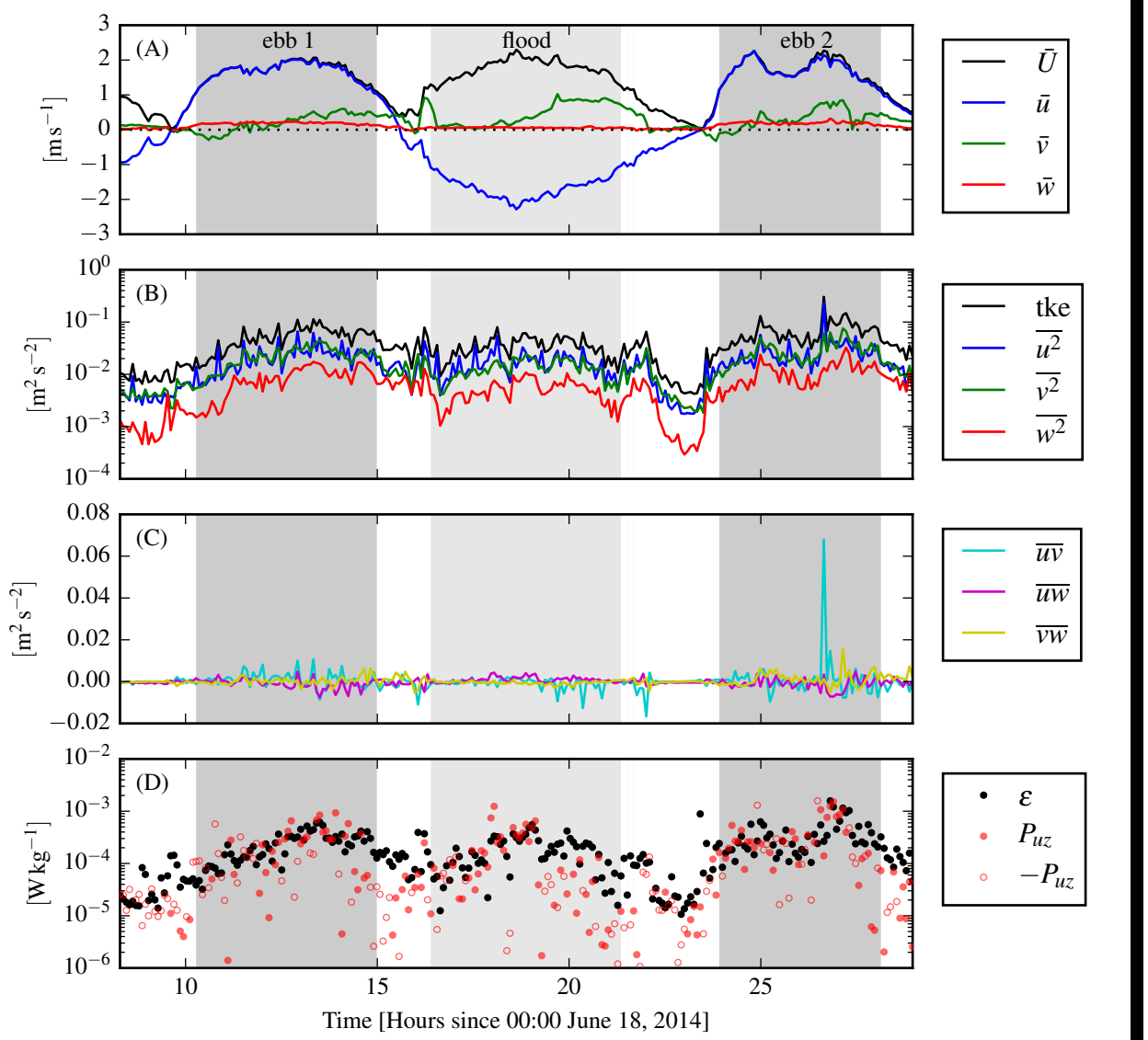
779 FIG. 11. Turbulence spectra from the turbulence torpedo during a 35-minute period when the mean velocity
 780 was 1.3 m s^{-1} . Annotations and line colors are identical to Figure 9.



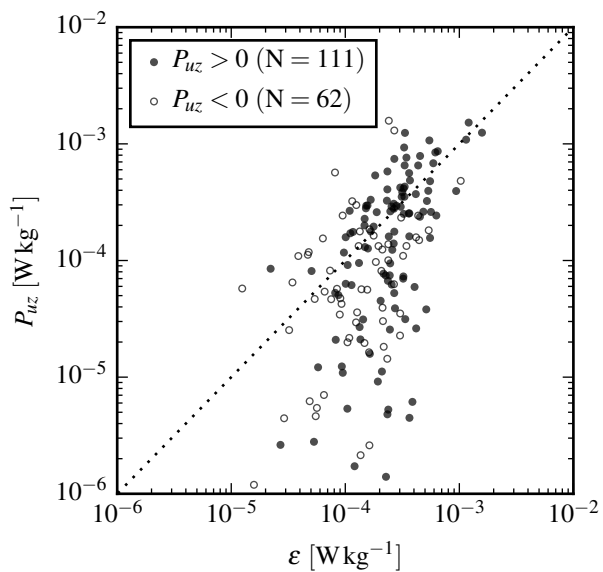
781 FIG. 12. Variance preserving cross-spectra between components of \mathbf{u} (blue), \mathbf{u}_h (red), and \mathbf{u}_m (black) from
 782 the June 2014 TTM deployment. The upper row is $fC\{\mathbf{u}, \mathbf{v}\}$, the middle row is $fC\{\mathbf{u}, \mathbf{w}\}$, and the bottom row
 783 is $fC\{\mathbf{v}, \mathbf{w}\}$ (also indicated at right). Note that these cross-spectra are between components of a velocity vector
 784 (e.g., \mathbf{u}), not between different vectors (i.e., not between \mathbf{u} and \mathbf{u}_m). N is the number of spectral ensembles in
 785 this average, i.e. when $2 < |\mathbf{u}| < 2.5 \text{ m s}^{-1}$. The light blue shading indicates one standard deviation of $fC\{\mathbf{u}\}$.



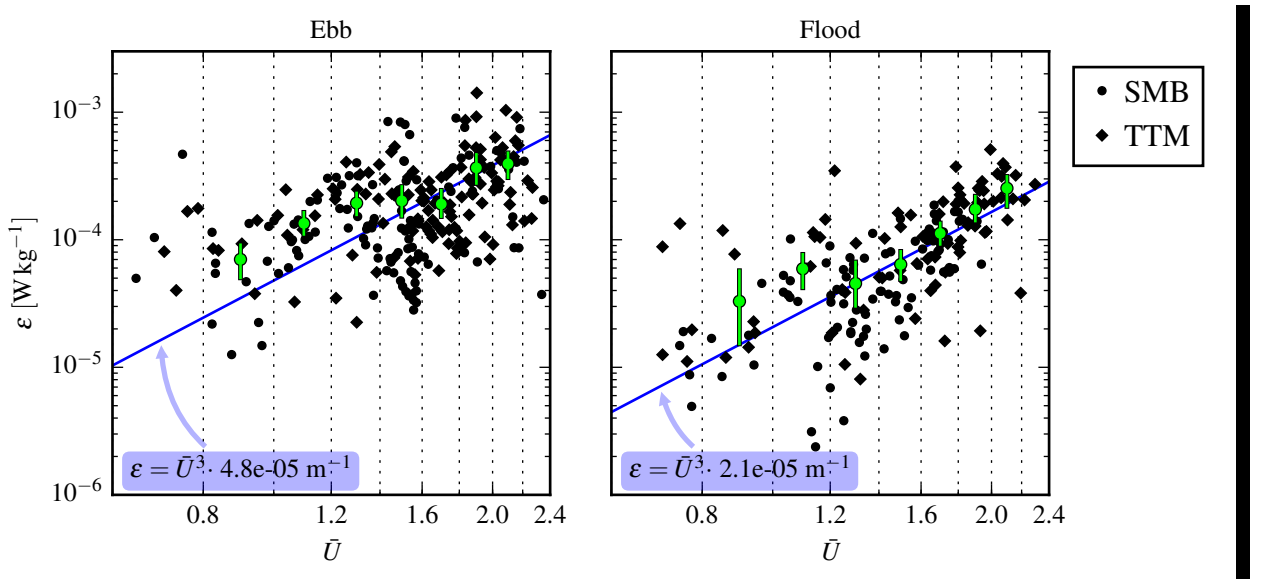
786 FIG. 13. Non-dimensional cross-spectra of motion corrected velocity, $\hat{C}\{u, w\}$, on a log-log scale. The average
 787 over $\Delta \hat{f} = 0.04$ bins is shown in blue, and single points are grey (negative values not shown). The semi-empirical
 788 Kaimal et al. (1972) form is shown as a thick black line, and the red dashed line indicates a $\hat{f}^{-7/3}$ slope. Cross-
 789 spectral estimates from measurements from a fixed ‘tripod’ are in purple.



790 FIG. 14. Time series of mean velocities (A), turbulence energy and its components (B),
 791 Reynold's stresses (C), and turbulence dissipation rate (D) measured by the TTM during the June 2014 deployment. Shading indicates
 792 periods of ebb ($\bar{u} > 1.0 \text{ ms}^{-1}$, grey) and flood ($\bar{u} < -1.0 \text{ ms}^{-1}$, lighter grey).



793 FIG. 15. P_{uz} vs. ϵ during the June 2014 TTM deployment for values of $|u| > 1$ m/s. Values of negative
794 production are indicated as open circles.



795 FIG. 16. A log-log plot of ε vs. \bar{U} for the June 2014 TTM (diamonds) and May 2015 SMB (dots) deployments,
 796 during ebb (left) and flood (right). Black points are 5-minute averages. Green dots are mean values within
 797 speed bins of 0.2 m s^{-1} width that have at least 10 points (50 minutes of data); their vertical bars are 95%
 798 bootstrap confidence intervals. The blue line shows a \bar{U}^3 slope, wherein the proportionality constant (blue box)
 799 is calculated by taking the log-space mean of ε/\bar{U}^3 .